DOI:
10.1109/TCI.2016.2557069

Document Version
Peer reviewed version

This article has been accepted for publication in a future issue of this journal, but has not been fully edited. Content may change prior to final publication. Citation information: DOI 10.1109/TCI.2016.2557069, IEEE Transactions on Computational Imaging

Sensitivity encoding for aligned multishot magnetic resonance reconstruction

Lucilio Cordero-Grande, Rui Pedro A. G. Teixeira, Emer J. Hughes, Jana Hutter, Anthony N. Price, and Joseph V. Hajnal

***Abstract*—This paper introduces a framework for the reconstruction of magnetic resonance images in the presence of rigid motion. The rationale behind our proposal is to make use of the partial k-space information provided by multiple receiver coils in order to estimate the position of the imaged object throughout the shots that contribute to the image. The estimated motion is incorporated into the reconstruction model in an iterative manner to obtain a motion-free image. The method is parameter-free, does not assume any prior model for the image to be reconstructed, avoids blurred images due to resampling, does not make use of external sensors, and does not require modifications in the acquisition sequence. Validation is performed using synthetically corrupted data to study the limits for full motion-recovered reconstruction in terms of the amount of motion, encoding trajectories, number of shots and availability of prior information, and to compare with the state of the art. Quantitative and visual results of its application to a highly challenging volumetric brain imaging cohort of 207 neonates are also presented, showing the ability of the proposed reconstruction to generally improve the quality of reconstructed images, as evaluated by both sparsity and gradient entropy based metrics.**

***Index Terms*—magnetic resonance, image reconstruction, motion correction, parallel imaging, multishot acquisition**

I. Introduction

MAGNETIC resonance (MR) is a flexible but relatively slow imaging technique. Thus, for common acquisition requirements, motion can occur within the duration of an MR scan. Therefore, there is a demand for methods to prevent or correct for motion. In *multishot* or *segmented* methods, only a fraction of the k-space is acquired after a single radiofrequency (RF) excitation or, for magnetization prepared sequences, after a single preparation phase. This type of sampling usually provides a good compromise between true single-echo sequences, which are very slow, and single-shot sequences, which have limited resolution and less flexible contrast. However, the encoding requirements for high-resolution volumetric imaging imply that a large number of shots is required. As these shots are usually acquired distant in time [1], when motion occurs in between them, the images may be severely degraded.

Motion in MR imaging can be classified into rigid and non-rigid. Focusing on brain imaging, rigid motion is caused by patient head motion whereas non-rigid motion comes either from internal sources such as arterial pulsation or from other structures in the field of view (FOV) such as in cases of eyeball or neck motion. In this paper we propose a framework to correct for rigid motion during brain structural scans. Direct applications of the method include studies of severely diseased, non-compliant, elderly or pediatric patients. In addition, a high prevalence of motion artifacts has been reported in clinical examinations [2]. Finally, small motion will become a limiting factor for ultra-high resolution images. In this scenario, image quality improvement is to be expected from the application of motion compensation techniques even in cases where no perceptible motion artifacts are present [3].

From the vast literature on motion compensation in MR (see [4] for a review), we restrict ourselves to retrospective rigid motion correction methods in structural multishot MR. In [5], inconsistencies in k-space are detected by using parallel reconstruction of k-space subsets and corrupted lines are removed in order to perform the final reconstruction. This method is extended in [6] by the introduction of prior information using the projection onto convex sets formalism, allowing for an improvement both in terms of detection of inconsistencies and reconstruction error. Alternatively, in [7] a scheme is proposed in which the motion is extracted from a navigator built into the k-space sampling scheme, which is exemplified by using a spiral trajectory with low resolution navigator images that are registered to a reference. Related motion resilient approaches relying on a specific encoding trajectory have been proposed in [8] —using the implicit navigators provided by the periodically rotated overlapping parallel lines with enhanced reconstruction (PROPELLER) sampling scheme— and [9] (using radial trajectories). A more comprehensive treatment that uses all the acquired data without resorting to explicit or implicit navigators is introduced in [10]. Similarly to our proposal, the authors present a joint reconstruction and motion estimation method, but in their case reconstruction and motion estimation are formulated using distinct functionals,

Manuscript received April 18, 2016.

The authors acknowledge financial support from the European Research Council under the European Union's Seventh Framework Programme (FP/2007-2013) / ERC Grant Agreement n. 319456. This work was also supported by the Medical Research Council (MRC) (grant number MR/K0006355/1) and the Department of Health via the National Institute for Health Research (NIHR) Biomedical Research Centre based at Guy's and St Thomas' NHS Foundation Trust and King's College London. The views expressed are those of the authors and not necessarily those of the NHS, the NIHR or the Department of Health. The authors also acknowledge the mothers and the babies participating in the study, the Department of Perinatal Imaging & Health and the staff of the Neonatal Unit and post-natal wards, Guy's and St Thomas' NHS Foundation Trust. Thanks are also due to Alexander Loktyushin for providing the source code and advice about implementation details of his method.

The authors are with the Centre for the Developing Brain and Department of Biomedical Engineering, Division of Imaging Sciences and Biomedical Engineering, King's College London, King's Health Partners, St. Thomas' Hospital, London, SE1 7EH, UK. e-mails: {lucilio.cordero_grande, rui.azeredo_gomes_teixeira, emer.hughes, jana.hutter, anthony.price, jo.hajnal}@kcl.ac.uk.

This article has been accepted for publication in a future issue of this journal, but has not been fully edited. Content may change prior to final publication. Citation information: DOI 10.1109/TCI.2016.2557069, IEEE Transactions on Computational Imaging

as the former is based on the fidelity to the measured data whereas the latter is based on the minimization of a gradient entropy metric in the image domain. Complementarily, our approach makes use of the full reconstruction inverse to integrate multicoil information and estimate and correct for motion. As we will show in Section III-E, these extensions may potentially allow for larger ranges in motion recovery. In a recent step further [11], the same authors have extended the previous approach to use the fidelity to the measured data for elastic motion estimation. Nevertheless, once again, their proposal uses an approximation to the reconstruction inverse and the inclusion of multicoil information is not explicitly addressed. Finally, although applied to physiological motion correction, we should mention the related contribution in [12], which formulates the reconstruction and motion estimation problem jointly and in a parallel imaging scenario. However, their method is devised for free form deformations rather than rigid motion. Thus, the estimation is based on optical flow, which implies imaginary component truncation when applied to complex data reconstruction. Also, the aperture problem forces joint motion estimation and reconstruction to be constrained by a regularization term, which is not required within a rigid motion assumption.

In this paper we propose a general framework for rigid motion corrected reconstructions in volumetric MR acquisitions, which admits a simpler formulation than in multislice counterparts, where treatment of through-plane motion appears more intricate [4]. The contributions of our proposal are threefold: (1) we provide a fully data-based generalized reconstruction formulation where a common functional is used to estimate the rigid motion and the structural data in parallel MR using the sensitivity encoding (SENSE) redundancy the coil array provides, (2) we make use of a rigid transformation representation that fully preserves the image resolution, thereby allowing for optimal reconstructions when neglecting the non-rigid motion components[1], and (3) we study the regime in which these fully rigidly corrected reconstructions are possible in terms of the amount of motion, encoding trajectories, number of shots and use of prior information. In addition, the source code of a MATLAB implementation of the reconstruction method proposed in Section II together with the experiments in Section III is freely available at https://github.com/mriphysics/alignedSENSE.

The paper is organized as follows: In Section II we present the formulation for joint rigid motion estimation and image reconstruction for parallel multishot MR. In Section III we study both the motion estimation and reconstruction performance of the method with regard to the motion level, encoding trajectories, number of shots, use of prior information, and in relation to the results provided by [10]. In Section IV we explain, assess and illustrate its application in a real scenario, namely, the motion-corrected reconstruction of volumetric MR in neonatal brain imaging. In Section V we discuss the implications of our proposal together with its potential applicability and future developments. Finally, the main conclusions of this work are established in Section VI.

[1]We will refer to these optimal reconstructions as *fully rigidly corrected reconstructions*. They satisfy two properties: (a) true synthetic rigid motion parameters are estimated by the method and (b) reconstruction is performed using the aforementioned rigid transform representation.

II. Theory

In this Section we provide the high level formulation for multishot reconstruction in the presence of rigid motion (also referred to in this paper as *aligned reconstruction*), describe the elements involved in the formulation, paying special attention to the rigid motion transformation, and establish the problem solving procedure adopted.

A. Generalized rigid motion-corrected multishot reconstruction

The generalized reconstruction with rigid motion correction for parallel multishot imaging can be formulated in matrix form as:

$$(\hat{\mathbf{x}}, \hat{\mathbf{T}}) = \underset{\mathbf{x},\mathbf{T}}{\operatorname{argmin}} \|\mathbf{A}\boldsymbol{\mathcal{F}}\mathbf{S}\mathbf{T}\mathbf{x} - \mathbf{y}\|_2^2, \tag{1}$$

where $\mathbf{y}$ denotes the measured k-space data, $\mathbf{x}$ the image to be reconstructed, $\mathbf{T}$ the rigid motion transformation matrix, $\mathbf{S}$ the coil sensitivity matrix, $\boldsymbol{\mathcal{F}}$ the Discrete Fourier transform (DFT) encompassing applied k-space oversampling or downsampling, and $\mathbf{A}$ a sampling matrix. The forward model for this formulation, originally proposed in [13] for the estimation of $\mathbf{x}$ assuming $\mathbf{T}$ is known, is depicted in Fig. 1 and the different terms are described in Section II-B.

B. Model terms

We want to reconstruct a 3D image of size $N = N_1N_2N_3$, with N_l the number of voxels along dimension l using a coil array of C elements from $M = ESC$ samples of a discretized k-space grid of size $K = K_1K_2K_3$, where E denotes the number of sampled points per shot and S is the number of shots. The different terms included in (1) can be represented by the following matrices:

- $\mathbf{y}$ is a vector of size $M \times 1$.
- $\mathbf{A}$ is a matrix of size $M \times KSC$ given by $\mathbf{A} = \begin{bmatrix} \mathbf{A}_{11} & \cdots & \mathbf{0} & \cdots & \mathbf{0} \\ \vdots & \ddots & \vdots & \vdots & \vdots \\ \mathbf{0} & \cdots & \mathbf{A}_{1C} & \cdots & \mathbf{0} \\ \vdots & \vdots & \vdots & \ddots & \vdots \\ \mathbf{0} & \cdots & \mathbf{0} & \cdots & \mathbf{A}_{SC} \end{bmatrix}$ where $\mathbf{A}_{sc}$ is a matrix of size $E \times K$ that takes the value 1 if the sample e of the shot s corresponds to the k-space location indexed by k and 0 otherwise.
- $\boldsymbol{\mathcal{F}}$ is a matrix of size $KSC \times NSC$ given by $\boldsymbol{\mathcal{F}} = \begin{bmatrix} \boldsymbol{\mathcal{F}}_{11} & \cdots & \mathbf{0} & \cdots & \mathbf{0} \\ \vdots & \ddots & \vdots & \vdots & \vdots \\ \mathbf{0} & \cdots & \boldsymbol{\mathcal{F}}_{1C} & \cdots & \mathbf{0} \\ \vdots & \vdots & \vdots & \ddots & \vdots \\ \mathbf{0} & \cdots & \mathbf{0} & \cdots & \boldsymbol{\mathcal{F}}_{SC} \end{bmatrix}$ where $\boldsymbol{\mathcal{F}}_{sc} = \mathcal{F}_{N\rightarrow K}$ is a matrix[2] of size $K \times N$ representing a 3D DFT with applied oversampling or downsampling.

[2]We drop bold notation to avoid confusion with the DFT matrix applied in (1).

This article has been accepted for publication in a future issue of this journal, but has not been fully edited. Content may change prior to final publication. Citation information: DOI 10.1109/TCI.2016.2557069, IEEE Transactions on Computational Imaging

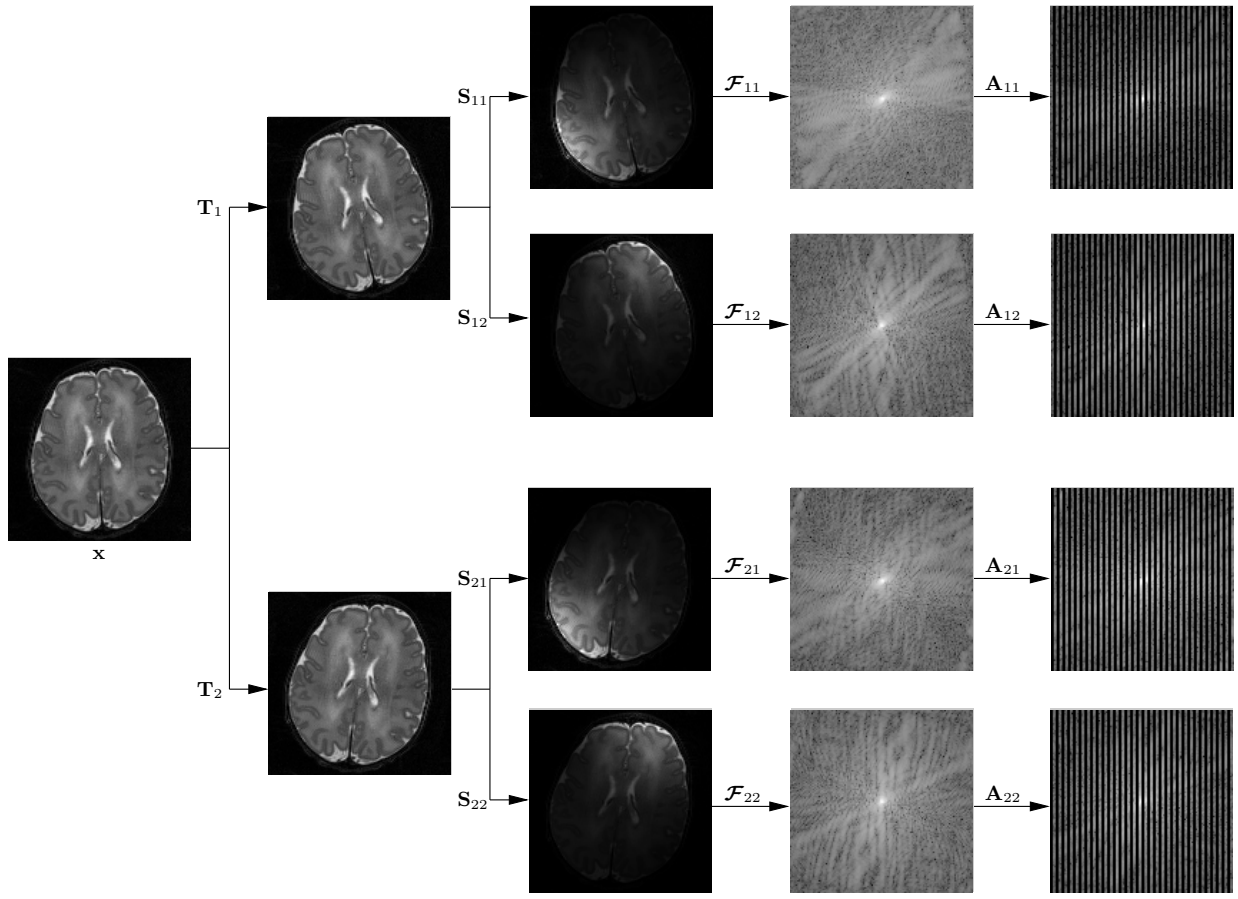

Fig. 1. Forward model (in 2D) of the measurement process in the presence of motion. The brain to be reconstructed $\mathbf{x}$ might be at different motion states $\mathbf{T}_s$ during the acquisition ($S = 2$ states are represented, which corresponds to a 2-shot acquisition). The coil receivers spatially encode the measured information by their sensitivity maps $\mathbf{S}_{sc}$ ($C = 2$ coils are assumed). The measurements are obtained in the Fourier space, so a DFT $\boldsymbol{\mathcal{F}}_{sc}$ is necessary. Finally, the data points sampled at each shot are extracted by means of $\mathbf{A}_{sc}$. A Cartesian acquisition without any spectral oversampling or downsampling is assumed in this example, where each shot is composed by every other vertical line (actually pairs of lines are grouped together for better visualization) so that the phase-encode direction is the horizontal one.

- $\mathbf{S}$ is a matrix of size $NSC \times NS$ given by $\mathbf{S} = \begin{bmatrix} \mathbf{S}_{11} & \cdots & \mathbf{0} \\ \vdots & \ddots & \vdots \\ \mathbf{S}_{1C} & \cdots & \mathbf{0} \\ \vdots & \ddots & \vdots \\ \mathbf{0} & \cdots & \mathbf{S}_{SC} \end{bmatrix}$, where $\mathbf{S}_{sc}$ is a diagonal matrix of size $N \times N$ whose diagonal elements correspond to the spatial profile of coil c.
- $\mathbf{T}$ is a matrix of size $NS \times N$ given by $\mathbf{T} = \begin{bmatrix} \mathbf{T}_1 \\ \vdots \\ \mathbf{T}_S \end{bmatrix}$, where $\mathbf{T}_s$ is a matrix of size $N \times N$ corresponding to the rigid transformation the underlying structure has been subject to when acquiring the shot s. This matrix is described just below.
- $\mathbf{x}$ is a vector of size $N \times 1$.

Regarding the functional form for $\mathbf{T}_s$, to the best of our knowledge, two representations have been used in the MR motion-corrected reconstruction literature. On the one hand, in [13] and [12], a sparse matrix is assumed with its non-zero elements given by the interpolation kernels used to spatially regrid the image after the transformation. On the other hand, in [7] and [10], the transformation is applied in k-space. In this case, translations can be expressed by linear phase weights but, once again, regridding is necessary to implement rotations. In contrast, our approach is based on the convolution-based interpolation technique introduced in [14], [15] in order to perform high quality rotations without any regridding. Thus, considering the decomposition of a rotation into three consecutive shears given in [14],

$$\begin{bmatrix} \cos(\theta) & -\sin(\theta) \\ \sin(\theta) & \cos(\theta) \end{bmatrix} = \begin{bmatrix} 1 & -\tan(\theta/2) \\ 0 & 1 \end{bmatrix} \begin{bmatrix} 1 & 0 \\ \sin(\theta) & 1 \end{bmatrix} \begin{bmatrix} 1 & -\tan(\theta/2) \\ 0 & 1 \end{bmatrix}, \tag{2}$$

a rigid transformation in 3D can be represented as a series of linear phase modulations in k-space by:

$$\begin{aligned} \mathbf{T}_s = \mathcal{F}^H \mathbf{U}_s \mathcal{F} \quad & \mathcal{F}_2^H \mathbf{V}_{1s}^{\tan} \mathcal{F}_2 \mathcal{F}_3^H \mathbf{V}_{1s}^{\sin} \mathcal{F}_3 \mathcal{F}_2^H \mathbf{V}_{1s}^{\tan} \mathcal{F}_2 \\ & \mathcal{F}_3^H \mathbf{V}_{2s}^{\tan} \mathcal{F}_3 \mathcal{F}_1^H \mathbf{V}_{2s}^{\sin} \mathcal{F}_1 \mathcal{F}_3^H \mathbf{V}_{2s}^{\tan} \mathcal{F}_3 \\ & \mathcal{F}_1^H \mathbf{V}_{3s}^{\tan} \mathcal{F}_1 \mathcal{F}_2^H \mathbf{V}_{3s}^{\sin} \mathcal{F}_2 \mathcal{F}_1^H \mathbf{V}_{3s}^{\tan} \mathcal{F}_1 \end{aligned} \tag{3}$$

where $\mathcal{F}$ represents the 3D DFT and $\mathcal{F}_l$ is the DFT along dimension l. The $\mathbf{U}_s$ and $\mathbf{V}_{ls}$ matrices are diagonal matrices of size $N \times N$ that describe, respectively, the applied translation

This article has been accepted for publication in a future issue of this journal, but has not been fully edited. Content may change prior to final publication. Citation information: DOI 10.1109/TCI.2016.2557069, IEEE Transactions on Computational Imaging

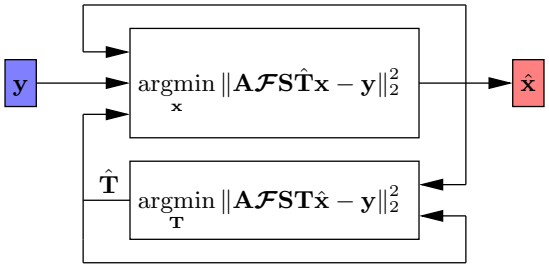

Fig. 3. Alternating minimization approach. As stated in (5), if $\mathbf{T}$ is assumed to be known, we can search for the best possible $\mathbf{x}$ in terms of the fidelity of the model to the measured data $\mathbf{y}$ and, conversely, assuming $\mathbf{x}$ is known, we can search for the best possible $\mathbf{T}$ using the same criterion.

and applied shear decomposed rotations along different axes, and whose diagonal vectors $\mathbf{u}_s$ and $\mathbf{v}_{ls}$ are given by:

$$\begin{aligned}
&\mathbf{u}_s = e^{-j(q_{1s}\mathbf{k}_1+q_{2s}\mathbf{k}_2+q_{3s}\mathbf{k}_3)} \\
&\mathbf{v}_{1s}^{\tan} = e^{j\tan(\theta_{1s}/2)\mathbf{k}_2\circ\mathbf{r}_3} \qquad \mathbf{v}_{1s}^{\sin} = e^{-j\sin(\theta_{1s})\mathbf{k}_3\circ\mathbf{r}_2} \\
&\mathbf{v}_{2s}^{\tan} = e^{j\tan(\theta_{2s}/2)\mathbf{k}_3\circ\mathbf{r}_1} \qquad \mathbf{v}_{2s}^{\sin} = e^{-j\sin(\theta_{2s})\mathbf{k}_1\circ\mathbf{r}_3} \\
&\mathbf{v}_{3s}^{\tan} = e^{j\tan(\theta_{3s}/2)\mathbf{k}_1\circ\mathbf{r}_2} \qquad \mathbf{v}_{3s}^{\sin} = e^{-j\sin(\theta_{3s})\mathbf{k}_2\circ\mathbf{r}_1}
\end{aligned} \tag{4}$$

where $\mathbf{k}_l$ is the k-space coordinate vector of the spectral image voxels along dimension l, $\mathbf{r}_l$ is the spatial coordinate vector of the image voxels along dimension l, $\circ$ denotes the Hadamard product, and $\mathbf{q}_s = q_{ls}$ and $\boldsymbol{\theta}_s = \theta_{ls}$ are, respectively, the translation parameters along the different dimensions and the rotation parameters along the different axes for each shot s.

One important property of this rigid transformation operator is its orthonormality, i.e., $\mathbf{T}_s^{-1} = \mathbf{T}_s^H$. This property is desirable when forward and backward application is required —see (6)— to avoid the introduction of blurring in the motion-corrected reconstructions. The application of this operator to a given image is illustrated in Fig. 2.

C. Problem solving

For the sake of computational tractability, the joint problem in (1) may be addressed in an alternating fashion (see Fig. 3) by iteratively solving the following subproblems:

$$\begin{aligned}
\hat{\mathbf{x}} &= \underset{\mathbf{x}}{\operatorname{argmin}} \|\mathbf{A}\boldsymbol{\mathcal{F}}\mathbf{S}\hat{\mathbf{T}}\mathbf{x} - \mathbf{y}\|_2^2 \\
\hat{\mathbf{T}} &= \underset{\mathbf{T}}{\operatorname{argmin}} \|\mathbf{A}\boldsymbol{\mathcal{F}}\mathbf{S}\mathbf{T}\hat{\mathbf{x}} - \mathbf{y}\|_2^2.
\end{aligned} \tag{5}$$

The first of these subproblems, i.e., that of reconstructing the image $\mathbf{x}$ in the presence of rigid motion, is considered in [13], where the system

$$\mathbf{T}^H\mathbf{S}^H\boldsymbol{\mathcal{F}}^H\mathbf{A}^H\mathbf{A}\boldsymbol{\mathcal{F}}\mathbf{S}\mathbf{T}\hat{\mathbf{x}} = \mathbf{T}^H\mathbf{S}^H\boldsymbol{\mathcal{F}}^H\mathbf{A}^H\mathbf{y} \tag{6}$$

is solved by means of the conjugate gradient (CG) algorithm.

The ability to estimate for motion (second subproblem) comes from the fact that the coil array measurements may be used to infer the position of the object inside the scanner using just partial k-space information. Mathematically, the reconstruction problem needs to be overdetermined for the motion estimation to be solvable. The solution must null the gradient of the objective function against the motion parameters:

$$\boldsymbol{\nabla}_{(\mathbf{q},\boldsymbol{\theta})}\|\mathbf{A}\boldsymbol{\mathcal{F}}\mathbf{S}\hat{\mathbf{T}}(\mathbf{q},\boldsymbol{\theta})\mathbf{x} - \mathbf{y}\|_2^2 = \mathbf{0}, \tag{7}$$

which can be solved separately for each shot,

$$\begin{aligned}
\frac{\partial\|\mathbf{A}_s\boldsymbol{\mathcal{F}}_s\mathbf{S}_s\hat{\mathbf{T}}_s(\mathbf{q}_s,\boldsymbol{\theta}_s)\mathbf{x} - \mathbf{y}_s\|_2^2}{\partial q_{ls}} &= 0 \\
\frac{\partial\|\mathbf{A}_s\boldsymbol{\mathcal{F}}_s\mathbf{S}_s\hat{\mathbf{T}}_s(\mathbf{q}_s,\boldsymbol{\theta}_s)\mathbf{x} - \mathbf{y}_s\|_2^2}{\partial \theta_{ls}} &= 0.
\end{aligned} \tag{8}$$

We have used the Newton's method for solving this system of equations. Details about the expressions of the gradient and Hessian as well as some remarks about the convergence criterion of the joint optimization can be found in Appendix A.

In the absence of additional information, a natural choice is a zero-motion initial condition $\mathbf{T}_s^0 = \mathbf{Id}$, thus making the first step of our method correspond to a standard CG SENSE reconstruction.

III. Validation

In this Section we perform a simulation-based study of the regime in which the proposed method can retrieve motion and, consequently, optimal reconstruction performance can be achieved in terms of the amount of motion, number of shots and encoding trajectory. In addition, we compare the performance of our approach with regard to a previous proposal [10].

A. Experimental design

Considering the immense range of potential sampling trajectories, acquisition orderings, patterns of motion and number of shots, we will initially restrict the simulation analysis to the 2D case. This way, we expect to identify the key factors that influence motion correction performance. Then, using the lessons learned by simulation, we will assess the 3D motion correction performance in Section IV, when applying the method in vivo. In order to replicate the expected anatomical features contained in a real image, a motion-free T_2 neonatal brain axial image is selected from a fast spin echo sequence with acquired pixel resolution 0.8×0.8 mm, 1.6 mm slice thickness, echo time $T_E = 145$ ms, repetition time $T_R = 12$ s and flip angle $\alpha = 90°$ using a head coil array with $C = 32$ channels on a 3 T Philips Achieva TX. Coil sensitivity maps were estimated from a separate reference scan using [16], which has been selected taking into account its robustness when extrapolating the sensitivities outside the calibrated region. The image has been reconstructed without zero filling, so that the resolution is maintained, and subsequently cropped to a 128×128 matrix so that the brain almost completely fills the FOV.

The resulting image is the one included in Fig 1. Our forward model of MR measurement in the presence of rigid motion has been applied to this image to generate synthetically motion corrupted data. We will study different degrees of motion as given by different rotations around the center of the FOV as a simple way to characterize the capture range of motion compensation. First, in Section III-B, we study the alternating minimization scheme performance for $S = 2$ shots using different encoding schemes and motion levels.

This article has been accepted for publication in a future issue of this journal, but has not been fully edited. Content may change prior to final publication. Citation information: DOI 10.1109/TCI.2016.2557069, IEEE Transactions on Computational Imaging

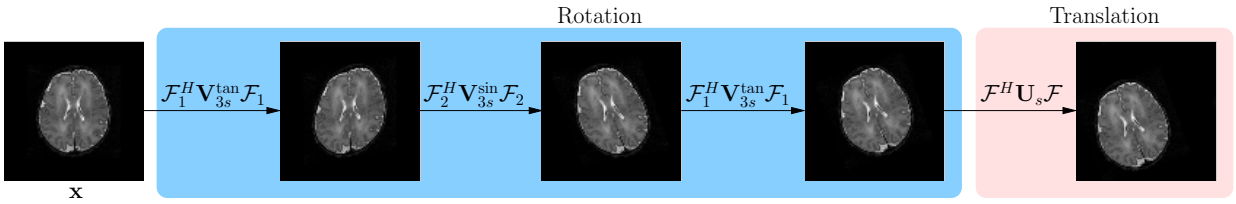

Fig. 2. Rigid transformation operator (in 2D). The rotation is composed of three consecutive shears applied in hybrid r/k-space whereas the translation is applied in k-space.

Then, in Section III-C, we focus on the isolated performance of the motion estimation (assuming $\mathbf{x}$ is perfectly known) and reconstruction (assuming $\mathbf{T}$ is perfectly known) parts. In Section III-D, we extend the analysis to characterize the behavior of the method for a larger number of shots. Finally, in Section III-E we study the differences in performance with the related approach in [10].

B. Influence of the encoding trajectory

In this Section, the performance of the method is studied for the following encoding schemes, which are illustrated in Fig. 4:

- A Cartesian sequential trajectory where k-space lines are acquired in increasing order so that the data points corresponding to a given shot form a connected region (Fig. 4a).
- A radial sequential trajectory where k-space locations are acquired in an order given by their orientation with respect to the center (Fig. 4b).
- A Cartesian parallel 1D trajectory where a shot consists of every other S line so that the lines of data points corresponding to a given shot are spread throughout k-space (Fig. 4c).
- A Cartesian parallel 2D trajectory where a shot consists of every other S location so that the data points corresponding to a given shot are arranged in a checkerboard-style fashion (Fig. 4d).
- A random trajectory where k-space is sampled following a random trajectory (Fig. 4e).

A simple experiment has been carried out in which a $S = 2$-shot acquisition is simulated, where a relative rotation of $\Delta\theta$ is assumed between shots. In Fig. 5, the reconstruction error as given by the value of the objective function f — the one to be minimized in (1), see also (10)— is plotted on a logarithmic scale against the logarithm of the number of iterations i of the joint optimization for each encoding scheme and $\Delta\theta = \{2°, 5°, 10°, 20°\}$. The reconstruction error is selected for assessment as it encompasses both the error in the estimated image relative to the ground truth and the error in the estimated motion parameters against their ground truth values. The results reflect that, for $\Delta\theta = 2°$, the convergence for parallel and random encodings is much faster than for sequential encodings. Indeed, the former ones provide a fully rigidly corrected reconstruction (up to numerical precision) in an affordable time whereas the latter ones take a much larger number of iterations to achieve an optimum (or to satisfy a reasonable stopping criteria in the context of this experiment). Something similar can be concluded from the results for $\Delta\theta = 5°$ where the parallel 2D appears to have the best convergence properties, followed by the parallel 1D and random encodings. In this case the radial sequential strategy seems unable to support a large decrease of the objective function value from its starting point. For $\Delta\theta = 10°$ the same convergence behavior as for $\Delta\theta = 5°$ is observed for the parallel and random encodings whereas, although there is a slight decrease in the objective function values, no perceptible improvements over reconstruction without motion correction are observed in any of the sequential encodings. Finally, for $\Delta\theta = 20°$ the proposed methodology is unable to recover from motion regardless of the encoding strategy adopted. Also, this case illustrates the relative salience of motion artifacts introduced by different encoding methods. As confirmed by the value of the objective function at the first iteration, sequential encodings seem to impact the image quality to a lesser extent than parallel and random encodings. Interestingly, the image degradation ranking of encoding methods relates inversely to their suitability for successful motion correction by the algorithm. This is further showcased in Fig. 6, where we compare the image appearance with and without alignment respectively for Cartesian sequential and Cartesian parallel 1D encodings, selected as representative of sequential and parallel encodings. First, we can see the incremental effect of motion artifacts from $\Delta\theta = 5°$ (Figs. 6a and 6b) to $\Delta\theta = 10°$ (Figs. 6c and 6d). Second, motion corruption artifacts in parallel encoding (Figs. 6b and 6d) appear much more coherent than their sequential counterparts (Figs. 6a and 6c). Third, motion corrected reconstruction is able to fully recover the uncorrupted ground truth both for sequential and parallel encodings for $\Delta\theta = 5°$ (respectively on Figs. 6e and 6f). However, despite aligned reconstructions are also obtained for $\Delta\theta = 10°$ in the parallel sampling case (Fig. 6h), almost no improvement is achieved for the same level of motion when using sequential encoding (Fig. 6g).

C. Potential benefits of the inclusion of prior information

Motion-corrected MR reconstruction has commonly been based on introducing certain assumptions about the image to be reconstructed, $\mathbf{x}$, such as its compact support and smooth phase, to help motion estimation and/or reconstruction [6]. In this Section we study the potential added value of introducing prior models about the image to be reconstructed in our framework by quantifying the capture range change of the motion estimation approach in the experimental conditions described in Section III-B. To this end, we study the motion estimation

This article has been accepted for publication in a future issue of this journal, but has not been fully edited. Content may change prior to final publication. Citation information: DOI 10.1109/TCI.2016.2557069, IEEE Transactions on Computational Imaging

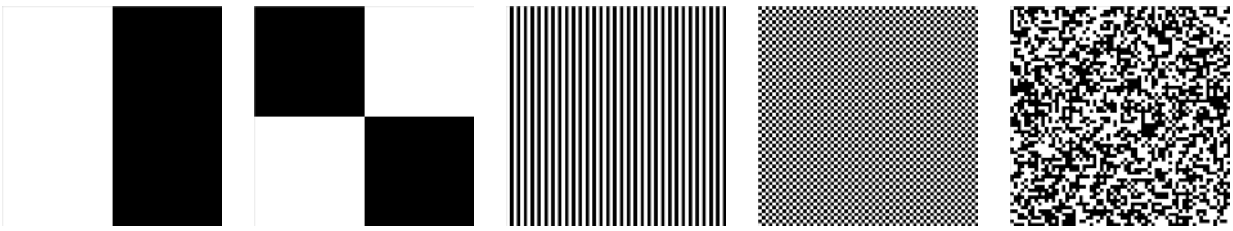

(a) Cartesian sequential. (b) Radial sequential. (c) Cartesian parallel 1D. (d) Cartesian parallel 2D. (e) Random.

Fig. 4. Considered encoding strategies exemplified for $S = 2$ shots: samples corresponding to one of the shots in white and those corresponding to the other in black.

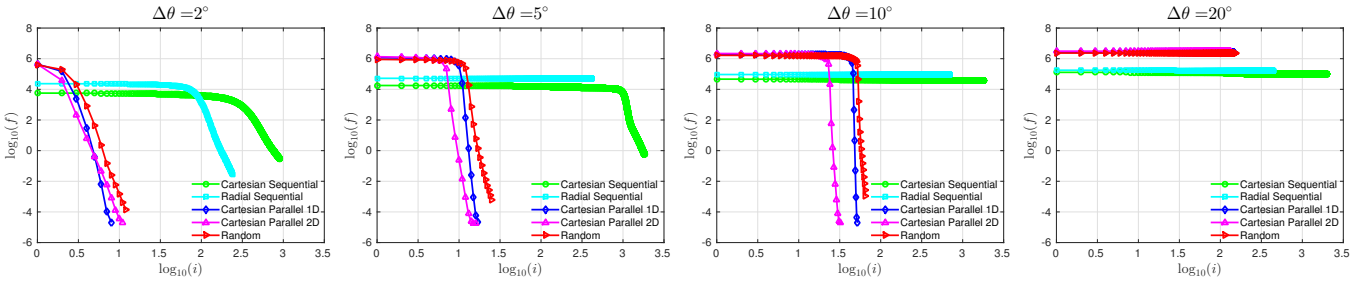

Fig. 5. Convergence curves of the objective function for different encoding strategies for $S = 2$ and different $\Delta\theta$. Note the logarithmic ordinate scaling, which implies that, whenever the curves start to decrease rapidly (as a rule of thumb, when they reach negative values), fully rigidly corrected reconstructions have been achieved.

step of our method assuming we have a perfect knowledge of $\mathbf{x}$ (i.e., best possible prior for $\mathbf{x}$). In accordance with the analysis of Section III-B we will focus on Cartesian sequential and Cartesian parallel 1D encodings, two characteristic cases that can illustrate the behavior for other encodings.

In Fig. 7 we show the motion estimation error as given by the logarithm of the objective function f using the known $\mathbf{x}$ and the estimated transformation $\mathbf{T}$ versus the logarithm of the number of iterations i for the two selected encoding schemes and $\Delta\theta = \{30°, 60°, 90°, 120°, 150° 180°\}$. As compared with the results in Fig. 5, the assumption of a perfect knowledge of the image to be estimated makes the motion estimation procedure less prone to get trapped in local optima, as the global optimum is achieved for $\Delta\theta \leq 150°$ for both encoding schemes. Thus, interestingly, a similar performance for sequential and parallel encodings is observed in this case. This seems to suggest that the relatively worse performance of the sequential encoding in the joint alignment and reconstruction case is related to the reconstruction step rather than to the alignment itself. This hypothesis has been tested by performing a new experiment in which the optimal $\mathbf{T}$ is assumed to be known (thereby assuming a perfect prior for $\mathbf{T}$) so that the reconstruction error using the estimated image $\mathbf{x}$ is assessed. Convergence when running $I = 100$ iterations is shown in Fig. 8 for the same configuration of encodings and levels of motion as in Fig. 7. As hypothesized, the parallel encoding method is able to fully recover the images in few iterations, whereas the sequential encoding struggles to do so. This behavior can be explained if one pays attention to the effect a relative rotation between shots would have in the k-space sampling structure of both encodings (we use here the 2-shot example of Figs. 4a and 4c for an intuitive explanation). Keeping in mind that a rotation in

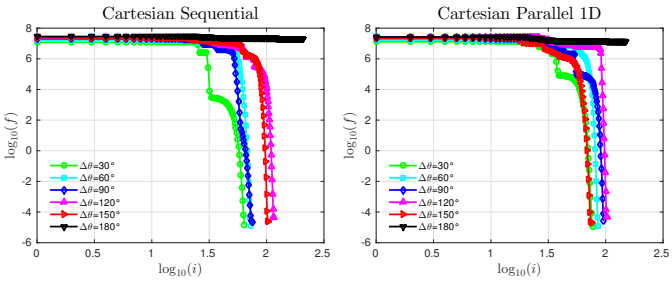

Fig. 7. Convergence curves of the objective function for $S = 2$ and different $\Delta\theta$ assuming optimal $\mathbf{x}$ is known. Note the logarithmic ordinate scaling, which implies that, whenever the curves start to decrease rapidly (as a rule of thumb, when they reach negative values), fully rigidly corrected reconstructions have been achieved.

space corresponds to a rotation in k-space, in the first case (sequential encoding) a given rotation would provoke a single unsampled connected region of k-space (as in this case the samples corresponding to a given shot are clustered together). In the second case (parallel encoding) the unsampled region after the same rotation would be comprised of many connected components, so that, in general, each of these components will be smaller in size than the single component of the sequential case. Thus, in the sequential case, the inversion problem will become more rapidly ill-posed, as the sensitivity based k-space deconvolution is highly unstable when far apart from the sampled regions due to the almost complete lack of high spatial frequency information of the coil profiles [17], whereas in the parallel case, the information of unsampled locations can be more easily retrieved with the aid of the low spatial frequency encoding information from the sensitivity maps.

This article has been accepted for publication in a future issue of this journal, but has not been fully edited. Content may change prior to final publication. Citation information: DOI 10.1109/TCI.2016.2557069, IEEE Transactions on Computational Imaging

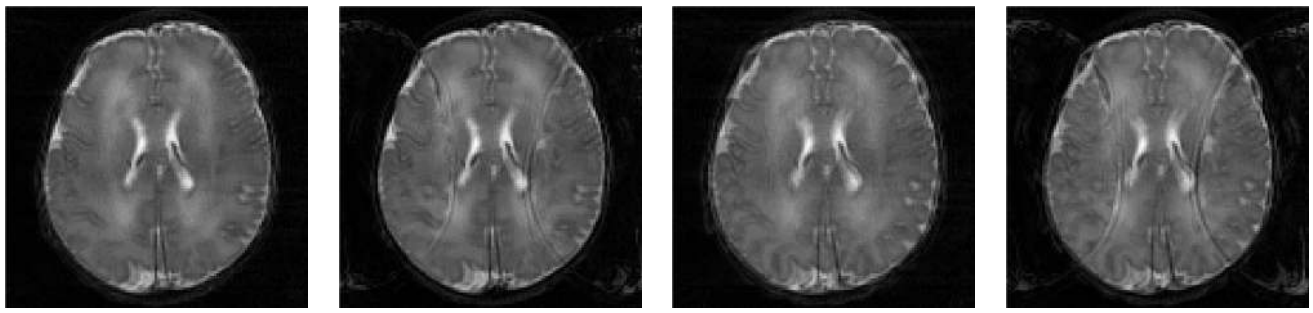

(a) Sequential uncorrected $\Delta\theta = 5°$. (b) Parallel uncorrected $\Delta\theta = 5°$. (c) Sequential uncorrected $\Delta\theta = 10°$. (d) Parallel uncorrected $\Delta\theta = 10°$.

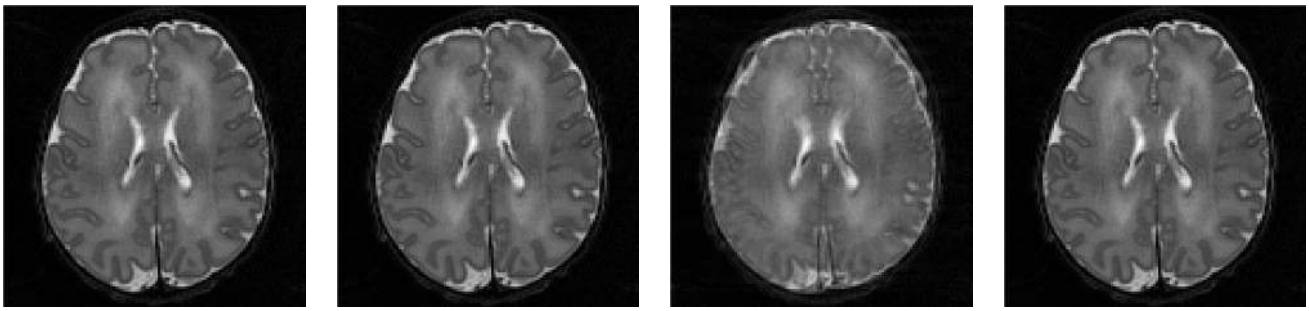

(e) Sequential Corrected $\Delta\theta = 5°$. (f) Parallel corrected $\Delta\theta = 5°$. (g) Sequential corrected $\Delta\theta = 10°$. (h) Parallel corrected $\Delta\theta = 10°$.

Fig. 6. Reconstructed images for $S = 2$ and different $\Delta\theta$ for Cartesian sequential and parallel 1D encodings. More coherent artifacts are observed for parallel encoding but fully rigidly motion corrected reconstructions are obtained for larger $\Delta\theta$ than in the sequential case.

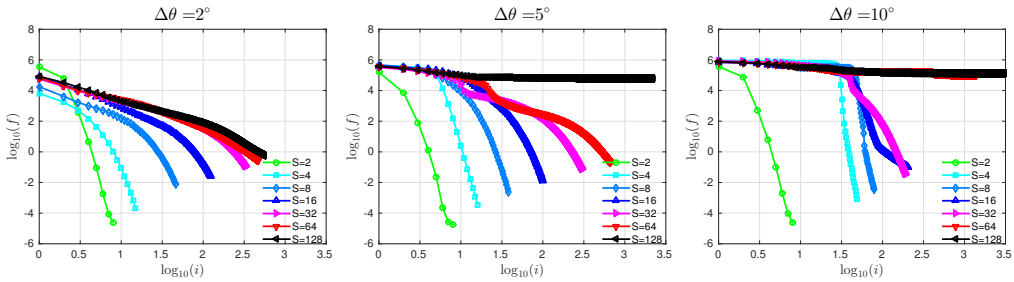

Fig. 9. Convergence curves of the objective function using the Cartesian parallel 1D encoding for different S and $\Delta\theta$. Note the logarithmic ordinate scaling, which implies that, whenever the curves start to decrease rapidly (as a rule of thumb, when they reach negative values), fully rigidly corrected reconstructions have been achieved.

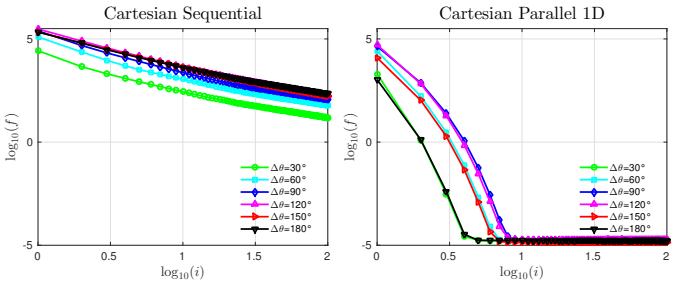

Fig. 8. Convergence curves of the objective function for $S = 2$ and different $\Delta\theta$ assuming optimal $\mathbf{T}$ is known. Note the logarithmic ordinate scaling, which implies that, whenever the curves start to decrease rapidly (as a rule of thumb, when they reach negative values), fully rigidly corrected reconstructions have been achieved.

D. Influence of the number of shots

In this Section we extend the analysis presented in Section III-B to the case of $S > 2$-shot acquisitions focusing on the Cartesian parallel 1D encoding strategy. In this case each shot will be affected by a rigid transformation sampled independently from a uniform distribution of rotations in the range $[-\Delta\theta/2, \Delta\theta/2]$ with subsequent subtraction of the mean rotation to deduct the drifting effect described at the end of Appendix A from the analysis. Results of the convergence of the algorithm are summarized in Fig. 9 for $\Delta\theta = \{2°, 5°, 10°\}$. The first conclusion is that the ability to correct for rigid motion seems to extend nicely when increasing the number of shots. Indeed, for the case $\Delta\theta = 10°$, which was the limit of good performance for $S = 2$, we can see that we can recover from motion up to $S = 32$, which means that just four lines are acquired per shot. Additionally, for minor motion corruption, as given by $\Delta\theta = 2°$, fully recovery has been possible even when just one line is acquired per shot ($S = 128$). We should clarify that these results are illustrative, as details may change when applying the method to different realizations of the rigid transform distribution. However, almost sure convergence is to be expected for small motion and number of shots and convergence will be almost

This article has been accepted for publication in a future issue of this journal, but has not been fully edited. Content may change prior to final publication. Citation information: DOI 10.1109/TCI.2016.2557069, IEEE Transactions on Computational Imaging

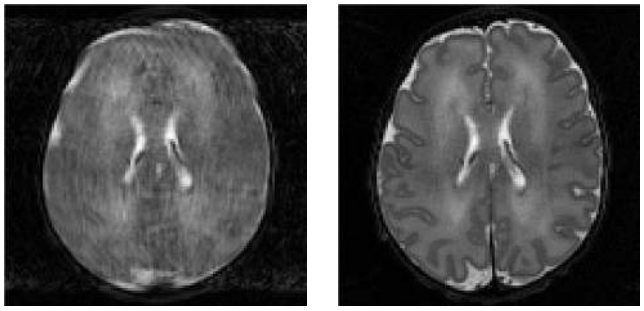

(a) Uncorrected $\Delta\theta = 10^\circ$. (b) Corrected $\Delta\theta = 10^\circ$.

Fig. 10. Reconstructed images for $S = 32$ and $\Delta\theta = 10^\circ$ for Cartesian parallel 1D encoding. Despite the dramatic damage to image structures, the result of our motion corrected reconstruction is identical to the ground truth (up to numerical precision).

impossible for large motion and number of shots. In Fig. 10 we include the resulting reconstructions without and with motion correction for $S = 32$ and $\Delta\theta = 10^\circ$. Despite the dramatic damage to image structures (Fig. 10a), the aligned reconstruction has been able to fully resolve them (Fig. 10b). Good performance of the method when applied to a large number of shots implies that motion estimation would be equally possible in accelerated acquisitions. A real application domain where the data acquisition has been accelerated by reduced phase-encode FOV and simultaneously decomposed into a large number of shots is described in Section IV.

E. Comparison with the state of the art

As stated in Section I, partial solutions for combined motion estimation and motion compensated reconstruction have been previously proposed. In this Section we perform a comparison of our results with one of such solutions [10]. This approach has been selected for comparison because of the closeness of its formulation to the one here proposed. Namely, [10] also uses a forward model of the acquisition process in the presence of motion as a way to obtain estimations of the rigid motion throughout the acquisition. Despite the publicly available implementation at http://mloss.org/software/view/430/ is just implemented for the single coil case, the authors have kindly provided us with their extension to the multicoil case, which is used in the comparisons presented here. On the other hand, as we want to compare the performance without assuming any temporal model for the rigid motion, we have disabled the term that accounts for the regularization of the trajectory of the recovered motion parameters. Finally, although the extension to other encoding scenarios would be conceptually simple, their current implementation assumes that one motion state has to be estimated per phase encode line. Thus, in order to cover the full regime of performance of our method, from convergence to the right solution to partial improvement, and simultaneously being able to run the current implementation of [10], we have assumed that motion occurs over the central portion of the k-space, namely over the central $S = 32$ lines of a parallel 1D encoding with one shot per line, so just this information is used for motion estimation. Comparisons are performed using the same motion distributions as in Section III-D for $\Delta\theta = \{0^\circ, 5^\circ, 20^\circ\}$. In Fig. 11 we show the error in the estimation of motion parameters for our method and [10].

Results for $\Delta\theta = 0^\circ$, which simulates a motion-free case, show that, whereas our method converges to the right solution, [10] is limited in providing optimal reconstructions for motion-free images. This is due to the fact that a different formulation is used for motion estimation and reconstruction. Thus, estimated motion parameters for motion-free images are generally not null. Although this error might have a minor effect in the quality of reconstructed images, it points to the fact that our method might be better envisaged as a natural extension of standard CG-SENSE reconstructions for motion-free cases, as, ideally, the motion corrected reconstructions would not introduce any side effect. Differences in performance are better understood by looking at the results for $\Delta\theta = 5^\circ$. In this case, partial improvement is obtained by using [10] as the estimated motion parameters error is generally lower than without performing any estimation (as given by the ground truth parameters, also depicted in Fig. 11 for reference). In contrast, exact estimation of motion parameters is obtained with our method, which, in combination with the reconstruction based on the unitary representation of rigid transforms, would provide fully rigidly corrected reconstructions. Finally, results for $\Delta\theta = 20^\circ$ show that, for relatively large motion, both methods provide partial corrections. However, the errors of our method are generally lower. In addition the error curves reveal another interesting feature. Whereas non-structured error curves are obtained using [10], structured errors are obtained in our case. We think that this effect, which suggests that the local minima of our formulation may contain part of the structure of the global minimum, could be related with the usage of multicoil information. The k-space convolution effect imposed by the sensitivity maps, might be helping to obtain piecewise consistent representations of the underlying motion. In addition, as discussed in [10], the use of the empirical inverse —constructed by neglecting the effect of the left hand side matrix in (6)— to estimate motion, would limit the ability to recover from large motion, where the empirical inverse approximation will no longer hold. In our case, as we use the full inverse, complete recovery is potentially possible.

In Fig. 12 we show a visual comparison of the appearance of partially recovered images for 1D parallel encoding with $S = 128$, $\Delta\theta = 5^\circ$, motion synthesized as described in Section III-D, and 1000 iterations of both methods (in order for their computation times to remain comparable). Quality of motion-corrected reconstructions compares favourably against non-corrected reconstructions for both methods. However, residual blurring is visible for [10], which should correspond to erroneous parameter estimation, whereas only minor artifacts (partly due to incomplete convergence) remain with our approach.

IV. Application

In this Section we present the application of the proposed method to the retrospective motion compensated reconstruction of a T_1-weighted 3D neonatal brain imaging sequence. In

This article has been accepted for publication in a future issue of this journal, but has not been fully edited. Content may change prior to final publication. Citation information: DOI 10.1109/TCI.2016.2557069, IEEE Transactions on Computational Imaging

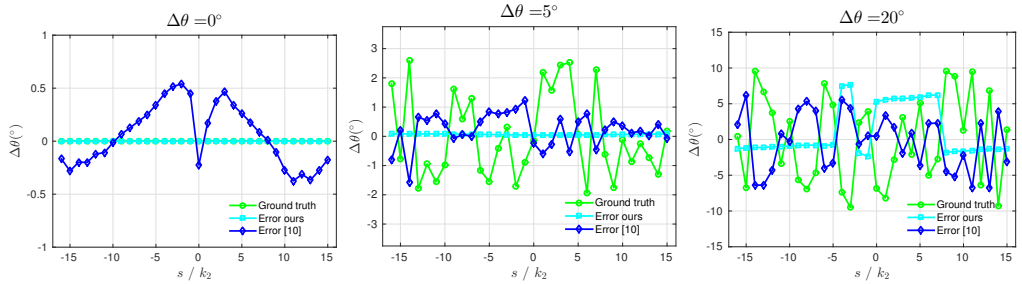

Fig. 11. Graphs of error in motion estimation parameters plotted against shot number (s) —alternatively k-space line number (k_2)— for the method in [10] and ours. Our method provides correct estimations of motion parameters in the motion-free (left) and moderate motion (center) cases and more consistent partial recovery for large motion (right).

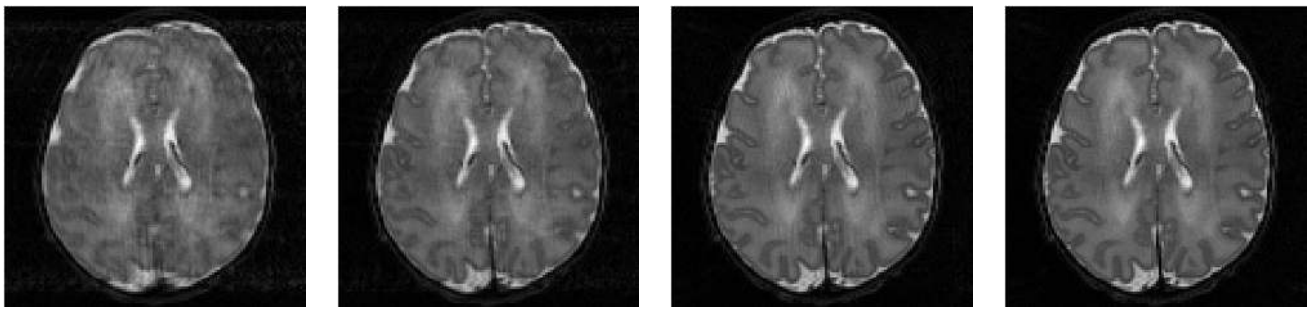

(a) Uncorrected. (b) Corrected using [10]. (c) Corrected using our method. (d) Ground truth.

Fig. 12. Comparison of reconstructed images with different motion correction methods for $S = 128$ and $\Delta\theta = 5°$.

Section IV-A we describe the details of the sequence and set of cases the method has been applied to, later, in Section IV-B, we describe certain implementation decisions adopted in this real case scenario, and, finally, in Section IV-C we summarize the obtained results.

A. Materials

Neonatal brains have been imaged in natural sleep using a magnetization prepared rapid acquisition gradient echo (MP-RAGE) sequence [18]. Even in these conditions, babies sporadically move, which damages the quality of reconstructed images. 3D T_1 images were acquired as part of a broader examination aimed to study brain development in a large number of neonates within the Developing Human Connectome Project (dHCP). Written informed consent was obtained for all participants prior to scanning. Neonatal informed consent was provided by someone with parental responsibility. All study procedures were reviewed and approved by the Riverside Research Ethics Committee (14/LO/1169). Multislice structural, functional and diffusion weighted magnetic resonance scans were also performed. Thereby, the acquisition time of the MP-RAGE data was limited to 275 s where a $135\times135\times108\,\text{mm}^3$, inferior-superior (IS) / anterior-posterior (AP) / left-right (LR) FOV was acquired with $0.8\,\text{mm}^3$ resolution. The phase encoding dimensions —AP (faster encoding) and LR (slower encoding)— are sampled using an elliptical k-space shutter with $S = 113$ shots and $E = 121$ samples per shot for a total of $K_2 = 181$, $K_3 = 113$ acquired samples and $N_2 = 181$, $N_3 = 135$ reconstructed samples, where subindexes 2 and 3 refer respectively to the AP and LR dimensions[3]. Thus, a SENSE factor of 1.19 is used in the LR dimension. A combination of Cartesian sequential (LR) and pseudorandom (AP) encoding strategies is applied. Acquisition parameters are selected as $T_R = 11\,\text{ms}$, $T_E = 4.6\,\text{ms}$, inversion time $T_I = 1.4\,\text{s}$, $\alpha = 9°$, and shot interval 2.075 s. The proposed reconstruction procedure is applied to a dataset of 207 babies with gestational ages ranging from $35 + 1$ to $42 + 2$ weeks, scanned using a 3 T PHILIPS ACHIEVA TX with a dedicated $C = 32$-channel neonatal head coil (RAPID BIOMEDICAL) and patient handling system [19]. As a preprocessing step of our method, coil sensitivity maps are estimated from a separate reference scan [16].

B. Implementation details

The main issue with the application of the proposed methodology to the dataset described in Section IV-A is the number of shots, $S = 113$, into which the acquisition is split. Aside from the inherent complexity of estimating the motion for each shot, this number of shots and the 3D nature of the problem introduce large computational requirements when applying the matrices described in Section II-B. Thus, several implementation arrangements have been introduced for the problem to become solvable in practice; namely:

- Coil information has been compressed using [20] so that just a 95% of the energy is preserved. This has reduced the effective number of coils from $C = 32$ to around

[3]As we are in a Cartesian setting, a fully sampled readout is obtained for each phase encode. This allows the readout dimension to be dropped from the formulation.

This article has been accepted for publication in a future issue of this journal, but has not been fully edited. Content may change prior to final publication. Citation information: DOI 10.1109/TCI.2016.2557069, IEEE Transactions on Computational Imaging

$C = 8$ (depending on the case) with minor impact in SNR and ability to resolve motion, as confirmed in all test cases in which full and compressed formulations were compared.

- A multiresolution strategy has been adopted which progressively incorporates high spatial frequency components into the formulation. Thus, at the grossest level the proposed method is applied to a low resolution version of the reconstruction problem (i.e., using only the low spatial frequencies). Then, the motion parameters and reconstructed image are propagated to the next level as the initializers of the reconstruction corresponding to that level. In our specific implementation, the structure of the multiresolution decomposition is designed in such a way that the grossest level of the pyramid preserves information about every shot so that at least one sampled point of every shot is included in the frequencies corresponding to that resolution level. This way, for the phase encoding described in Section IV-A, all frequencies have to be preserved in the slower phase encode direction (LR) and the pyramid is applied just on the first (IS) and second (AP) directions. 3 resolution levels have been used with a subsampling ratio of 2. The motion estimation step, which takes longer than the reconstruction step, is not applied at the finest scale to accelerate computations, as we have observed that the refinement it provides has an almost imperceptible impact on the obtained reconstructions when assessed over exemplary datasets.
- Due to the large number of shots, the usage of prior information about the image to be reconstructed seems advisable. However, the design of adequate priors for this reconstruction problem is out of the scope of our work. Thus, we have resorted to a simple method to slightly improve the ability to escape from local optima of the joint formulation which, on the basis of a compact support assumption, forces the reconstruction to be zero outside a spatial mask obtained from the reference scan used to compute the coil sensitivity maps. This mask is fixed for the reconstruction step but it is iteratively refined each time a new image is computed and applied to the solution image used in the motion estimation step.
- The rigid motion assumption may be violated in regions outside the brain such as the neck. Thus, the motion estimation part of our method may benefit from restricting the used information to a region containing only brain tissues. However, for the phase encoding directions, motion estimation is performed using k-space information, which inherently includes contributions from the whole FOV. Thereby, without departing from the basic formulation proposed here, the region containing the brain can only be extracted along the readout direction (IS), for which the estimation of the motion state corresponding to a given shot can be likewise performed using spatial or spectral information. A simple criteria in which a slab containing the upper half of the FOV is used for motion estimation has proven beneficial in our particular setting. This region of interest (ROI) extraction also helps in performing accelerated reconstructions.
- GPU processing is very well suited to the matrix multiplications and DFT operations involved in our reconstruction problem. Thereby, a GPU version of the algorithm has been used in practice.

With these arrangements, computation time using a GEFORCE GTX TITAN X GPU ranges from approximately 15 minutes in moderately degraded datasets to about 600 minutes in severely degraded datasets.

C. Assessment

Two metrics have been used to quantitatively assess the relative image quality of uncorrected and corrected reconstructions:

- One of them makes use of the recently introduced ideas in [21], where the authors propose to promote the sparsity of the reconstructed image in a properly selected domain as a criteria to compensate for motion. This idea is grounded on the conjecture that motion-corruption artifacts will degrade the compressibility of reconstructed images, which was numerically checked for the ℓ_1-norms of uncorrupted and corrupted images under a Haar wavelet decomposition. Here, we use the compressibility to construct a metric for assessing the ability to correct for motion in vivo. Namely, we compare $\|\boldsymbol{\mathcal{W}}^3_{\text{Db-}a}\mathbf{x}\|_1$, with $\boldsymbol{\mathcal{W}}^3_{\text{Db-}a}$ denoting the a-vanishing moments Daubechies (Db) wavelet decomposition at level 3, in uncorrected and corrected images.
- A more canonical metric, the gradient entropy (GE), has been selected on the basis of the results in [22], where this metric showed to have the strongest correlation with observer quality scores.

We perform a paired right-tailed sign test against the null hypothesis that the median of the difference of these metrics with and without motion correction is lower than zero or zero to assess whether the aligned reconstruction effectively improves the sparsity of the wavelet coefficients and minimizes the entropy of the reconstructed image gradient. The corresponding box plots, significance levels, and improvement ratio for each metric are included in Fig. 13.

Results are highly significant ($p \ll 0.05$) for all metrics. Namely, a 71.5% of cases for the GE metric and up to an 89.4% of cases for the wavelet metric are consistent with equal or improved image quality after motion correction (when assessing it by a decrease in the metric value). Therefore, performed tests show the ability of the motion correction method to effectively improve the compressibility and minimize the entropy of the gradient of reconstructed images, which, we interpret, is derived from its ability to reduce motion artifacts. However, in some of these cases there were other artifacts, such as unresolved SENSE folding, that also impacted image quality.

The performance of the method is illustrated by the visual results included in Fig. 14. First, in Fig. 14a we show the uncorrected and corrected reconstructions for a case in which no evident motion artifacts were present. In this motion-free scenario, motion-corrected images look almost identical to their motion-free counterparts, which provides evidence that

This article has been accepted for publication in a future issue of this journal, but has not been fully edited. Content may change prior to final publication. Citation information: DOI 10.1109/TCI.2016.2557069, IEEE Transactions on Computational Imaging

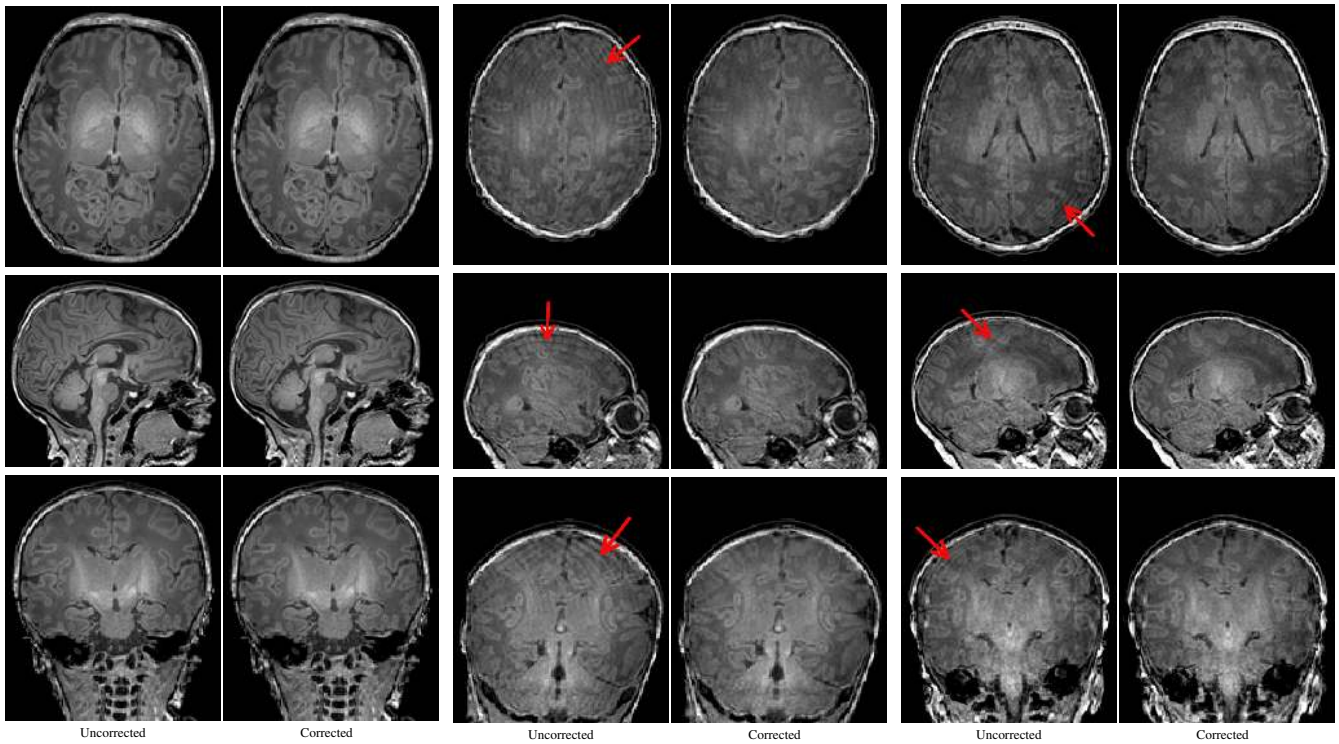

(a) No motion. (b) Substantial recovery. (c) Partial recovery.

Fig. 14. Visual results of aligned reconstruction of MP-RAGE sequences. Arrows point to areas with appreciable motion artifacts in the uncorrected images.

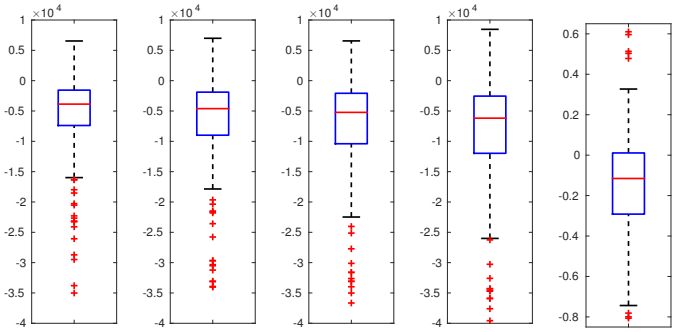

(a) Db-1 $p < 10^{-20}$ $r = 86.5\%$ (b) Db-2 $p < 10^{-20}$ $r = 88.4\%$ (c) Db-3 $p < 10^{-20}$ $r = 89.4\%$ (d) Db-4 $p < 10^{-20}$ $r = 89.4\%$ (e) GE $p = 10^{-10}$ $r = 71.5\%$

Fig. 13. Box plots, p-values of a paired right-tailed sign test, and percentage of cases r in which the metric decreased for the ℓ_1 norm of Db wavelet decompositions and for the GE in motion corrected versus uncorrected reconstructions. Negative values in the paired box plots indicate a decrease in the corresponding metrics when applying motion correction, which has been documented as associated with an improvement in image quality [21], [22].

no artifacts are introduced when the acquired data is free of motion. Second, in Fig. 14b we encounter a different case in which the uncorrected reconstruction is affected by substantial artifacts that hinder some of the actual structures in the image whereas the aligned reconstruction has greatly diminished the impact of these artifacts. The effects are noticeable in all views. Finally, in Fig. 14c we show another example where motion was degrading the image quality in the uncorrected images. In this case, although the aligned reconstruction helps to diminish data inconsistencies, residual damage is clearly noticeable in the motion corrected reconstructions (see, for instance, the region pointed by the arrow in the axial view).

V. Discussion

The method here presented is based on incorporating the estimation of the rigid motion states the imaged structure traverses throughout the acquisition process on top of a standard CG SENSE reconstruction. One important feature of our formulation is the use of a common functional for both rigid motion estimation and reconstruction, which provides a simple interplay between both problems and allows its general application for retrospective motion corrected reconstructions in parallel MR. In Section III we described the conditions for which motion can be retrieved in a controlled environment where a motion free image was synthetically corrupted. Namely we showed that, for parallel and random encodings, we could recover from up to 10° rotations in 2-shot acquisitions. We also showed that this result generalizes nicely to a larger number of shots (up to 32 for 128 acquired phase-encodes). Moreover, we characterized the great potential of using prior information about the image to be reconstructed to help motion estimation, as in this case we could estimate for up to 150° rotations between the shots. Finally, we showed that our method provides more consistent corrections than those obtained by [10]. Additionally, experiments described in Section IV, where a 3D neonatal brain imaging sequence acquired in the presence of motion was retrospectively reconstructed using our method, have provided both quantitative and visual evidence of improvement even in this challenging application.

As suggested in the introduction, our framework seems especially well-suited for coping with motion artifacts in ultra-

This article has been accepted for publication in a future issue of this journal, but has not been fully edited. Content may change prior to final publication. Citation information: DOI 10.1109/TCI.2016.2557069, IEEE Transactions on Computational Imaging

high resolution structural brain MR, where small motion artifacts will usually degrade the quality and prescribed resolution of the acquired images [3]. In this scenario, the application of motion correction without sacrificing the reconstructed resolution, as given by our rigid transformation formulation, would help in extending the boundaries of the fine grained brain structure that can be imaged. Also, the flexibility of the proposed technique, that can be applied for virtually any encoding strategy, allows its usage in new compressed sensing paradigms for resolution enhancement [23].

Many proposals have focused on prospective rigid motion correction methods. Particularly, impressive accuracy has been reported for optical tracking procedures [24]. In this regard, we should recall that our technique admits a straightforward combination with these sort of approaches. Namely, if we assume motion can be well approximated by using external sensors, we would be in a more favorable regime to perform further small-motion adjustments (for instance to mitigate cross-calibration errors [25]). Also, provided motion can be accurately estimated and k-space sampling can be assumed homogeneous enough, our retrospective reconstruction would have a negligible impact in the image quality, which would reduce the need to perform real time modifications to the acquisition sequence.

Extending the proposed methodology for treating both within- and through-plane motion in multislice acquisitions might be possible by modifying the sampling mask to also encompass slice excitations. However, the fact that in this case each sampled shot contains a combination of spatial and spectral information may cause certain spatial locations to be more densely sampled than others if through-plane motion is present. We are currently investigating the use of negative slice gaps and superresolution in order to cope with this. Also, acquisition of multiple views could be used to improve robustness against through-plane motion. Finally, the spin-history effect would play a role in this scenario, so that bias correction and outlier rejection techniques should also be considered. We believe that comprehensive approaches that have been presented for 3D motion-corrected reconstruction of single shot multislice datasets [26], [27] could be combined with the ideas presented here to effectively tackle the multishot multislice motion-corrected reconstruction problem. Non-rigid motion extension [12], [11] and application in multicontrast imaging [28], under dynamic changes in contrast [29], [30] or to accelerate dynamic acquisitions [30], [31], are also directions that require further research.

When a large number of motion states have to be resolved such as in the application described in Section IV, the introduction of prior information to guide the motion estimation seems advisable. In this regard, and just as an exemplary sketch of a potential procedure, the wavelet-based ℓ_1 metric used for assessment could be incorporated as a prior in the first iterations of the alternating reconstruction and motion estimation step in order to promote artifact-free reconstructions that, in turn, could be used to escape local optima of the joint functional. Later on, the use of prior information could be disabled in order to correct for fine-detail motion inconsistencies. Nevertheless, the inclusion of prior information in the joint reconstruction scheme remains outside the scope of this paper, so we have not performed any further study in this direction.

We should also stress that motion estimation might be compromised when large spectral undersampling is applied, so that the localization capabilities of the coil array might start to struggle in recovering from motion and foldings simultaneously. Motion corrected reconstruction in this setting may become particularly difficult when errors in the sensitivity estimation (primarily in large motion scenarios where the object might move outside the calibrated region) or additional artifacts that break the model assumptions are present. In this case, one may resort to the literature on SENSE reconstruction with tolerance to coil inaccuracies to generalize our proposal [32], [33], [34].

VI. Conclusion

We have introduced a flexible procedure to retrospectively correct for rigid motion artifacts when reconstructing multishot MR images which is grounded in the coil array sensitivity to the spatial location of the object being scanned even when only partial k-space information is available. The method uses a common functional to estimate motion and reconstruct and, in its basic formulation, it is parameter-free. Additionally, it does not require a prior image or temporal modeling of rigid motion nor the use of external sensors, although it may benefit from their availability. Moreover, it can be applied to any encoding scheme without introducing modifications in the acquisition sequence. Finally, our formulation minimizes blurring and regridding artifacts by using a unitary representation of rigid transforms. In this paper we have carried out a comprehensive validation of the performance of the method against different levels of motion, encoding schemes, numbers of shots, introduction of prior information, and alternative algorithms, using synthetically corrupted images, thereby featuring the regime on which fully rigidly corrected reconstructions are possible. We have also quantitatively and visually demonstrated the quality improvement obtained in brain neonatal MP-RAGE studies when applying our proposed reconstruction scheme. We are currently focused on the extension of the framework to multislice acquisitions. Future plans include its extension to elastic motion compensated reconstructions and to study the inclusion of different image and motion priors.

Appendix A
Newton's method for estimating motion

The estimation of the imaged object motion state when a given shot is acquired can be performed by solving (8), which, dropping the shot index s from the notation, can be rewritten as:

$$\begin{aligned} \frac{\partial \|\mathbf{A}\boldsymbol{\mathcal{F}}\mathbf{S}\hat{\mathbf{T}}(\mathbf{q},\boldsymbol{\theta})\mathbf{x}-\mathbf{y}\|_2^2}{\partial q_l} &= 0 \\ \frac{\partial \|\mathbf{A}\boldsymbol{\mathcal{F}}\mathbf{S}\hat{\mathbf{T}}(\mathbf{q},\boldsymbol{\theta})\mathbf{x}-\mathbf{y}\|_2^2}{\partial \theta_l} &= 0. \end{aligned} \tag{9}$$

Thus, if we write $\mathbf{z} = (z_1, z_2, z_3, z_4, z_5, z_6) = (q_1, q_2, q_3, \theta_1, \theta_2, \theta_3)$, the objective function of our motion

This article has been accepted for publication in a future issue of this journal, but has not been fully edited. Content may change prior to final publication. Citation information: DOI 10.1109/TCI.2016.2557069, IEEE Transactions on Computational Imaging

estimation problem is

$$f(\mathbf{z}) = \|\mathbf{A}\boldsymbol{\mathcal{F}}\mathbf{S}\mathbf{T}(\mathbf{z})\mathbf{x} - \mathbf{y}\|_2^2. \tag{10}$$

Then, we have

$$\nabla_l^f = \frac{\partial f(\mathbf{z})}{\partial z_l} = 2\Re(\mathbf{w}^H \mathbf{w}_{(l)}),$$
$$\text{where } \begin{cases} \mathbf{w} = & \mathbf{A}\boldsymbol{\mathcal{F}}\mathbf{S}\mathbf{T}(\mathbf{z})\mathbf{x} - \mathbf{y} \\ \mathbf{w}_{(l)} = & \mathbf{A}\boldsymbol{\mathcal{F}}\mathbf{S}\dfrac{\partial \mathbf{T}(\mathbf{z})}{\partial z_l}\mathbf{x} \end{cases} \tag{11}$$

and

$$H_{lm}^f = \frac{\partial^2 f(\mathbf{z})}{\partial z_l \partial z_m} = 2\Re(\mathbf{w}_{(l)}^H \mathbf{w}_{(k)} + \mathbf{w}^H \mathbf{w}_{(lm)}),$$
$$\text{where } \mathbf{w}_{(lm)} = \mathbf{A}\boldsymbol{\mathcal{F}}\mathbf{S}\frac{\partial^2 \mathbf{T}(\mathbf{z})}{\partial z_l \partial z_m}\mathbf{x}. \tag{12}$$

If we make

$$\begin{aligned} \mathbf{Q}(z_1, z_2, z_3) &= \mathcal{F}^H \mathbf{U}(z_1, z_2, z_3)\mathcal{F} \\ \mathbf{R}_1(z_4) &= \mathcal{F}_2^H \mathbf{V}_1^{\tan}(z_4)\mathcal{F}_2 \mathcal{F}_3^H \mathbf{V}_1^{\sin}(z_4)\mathcal{F}_3 \mathcal{F}_2^H \mathbf{V}_1^{\tan}(z_4)\mathcal{F}_2 \\ \mathbf{R}_2(z_5) &= \mathcal{F}_3^H \mathbf{V}_2^{\tan}(z_5)\mathcal{F}_3 \mathcal{F}_1^H \mathbf{V}_2^{\sin}(z_5)\mathcal{F}_1 \mathcal{F}_3^H \mathbf{V}_2^{\tan}(z_5)\mathcal{F}_3 \\ \mathbf{R}_3(z_6) &= \mathcal{F}_1^H \mathbf{V}_3^{\tan}(z_6)\mathcal{F}_1 \mathcal{F}_2^H \mathbf{V}_3^{\sin}(z_6)\mathcal{F}_2 \mathcal{F}_1^H \mathbf{V}_3^{\tan}(z_6)\mathcal{F}_1, \end{aligned} \tag{13}$$

we can rewrite (3) as

$$\mathbf{T}(\mathbf{z}) = \mathbf{Q}(z_1, z_2, z_3)\mathbf{R}_1(z_4)\mathbf{R}_2(z_5)\mathbf{R}_3(z_6). \tag{14}$$

The partial derivatives of $\mathbf{T}$ are then:

$$\frac{\partial \mathbf{T}(\mathbf{z})}{\partial z_l} = \begin{cases} \dfrac{\partial \mathbf{Q}(z_1, z_2, z_3)}{\partial z_l}\mathbf{R}_1(z_4)\mathbf{R}_2(z_5)\mathbf{R}_3(z_6),\ 1 \le l \le 3 \\ \mathbf{Q}(z_1, z_2, z_3)\mathbf{R}_1'(z_4)\mathbf{R}_2(z_5)\mathbf{R}_3(z_6),\ l = 4 \\ \mathbf{Q}(z_1, z_2, z_3)\mathbf{R}_1(z_4)\mathbf{R}_2'(z_5)\mathbf{R}_3(z_6),\ l = 5 \\ \mathbf{Q}(z_1, z_2, z_3)\mathbf{R}_1(z_4)\mathbf{R}_2(z_5)\mathbf{R}_3'(z_6),\ l = 6, \end{cases} \tag{15}$$

and

$$\frac{\partial^2 \mathbf{T}(\mathbf{z})}{\partial z_l \partial z_m} = \begin{cases} \dfrac{\partial^2 \mathbf{Q}(z_1, z_2, z_3)}{\partial z_l \partial z_m}\mathbf{R}_1(z_4)\mathbf{R}_2(z_5)\mathbf{R}_3(z_6) \text{ if } 1 \le l \le m \le 3 \\ \dfrac{\partial \mathbf{Q}(z_1, z_2, z_3)}{\partial z_l}\mathbf{R}_1'(z_4)\mathbf{R}_2(z_5)\mathbf{R}_3(z_6),\ 1 \le l \le 3,\ m = 4 \\ \dfrac{\partial \mathbf{Q}(z_1, z_2, z_3)}{\partial z_l}\mathbf{R}_1(z_4)\mathbf{R}_2'(z_5)\mathbf{R}_3(z_6),\ 1 \le l \le 3,\ m = 5 \\ \dfrac{\partial \mathbf{Q}(z_1, z_2, z_3)}{\partial z_l}\mathbf{R}_1(z_4)\mathbf{R}_2(z_5)\mathbf{R}_3'(z_6),\ 1 \le l \le 3,\ m = 6 \\ \mathbf{Q}(z_1, z_2, z_3)\mathbf{R}_1''(z_4)\mathbf{R}_2(z_5)\mathbf{R}_3(z_6),\ l = m = 4 \\ \mathbf{Q}(z_1, z_2, z_3)\mathbf{R}_1'(z_4)\mathbf{R}_2'(z_5)\mathbf{R}_3(z_6),\ l = 4,\ m = 5 \\ \mathbf{Q}(z_1, z_2, z_3)\mathbf{R}_1'(z_4)\mathbf{R}_2(z_5)\mathbf{R}_3'(z_6),\ l = 4,\ m = 6 \\ \mathbf{Q}(z_1, z_2, z_3)\mathbf{R}_1(z_4)\mathbf{R}_2''(z_5)\mathbf{R}_3(z_6),\ l = m = 5 \\ \mathbf{Q}(z_1, z_2, z_3)\mathbf{R}_1(z_4)\mathbf{R}_2'(z_5)\mathbf{R}_3'(z_6),\ l = 5,\ m = 6 \\ \mathbf{Q}(z_1, z_2, z_3)\mathbf{R}_1(z_4)\mathbf{R}_2(z_5)\mathbf{R}_3''(z_6),\ l = m = 6 \end{cases} \tag{16}$$

where

$$\frac{\partial \mathbf{Q}(z_1, z_2, z_3)}{\partial z_l} = \mathcal{F}^H \frac{\partial \mathbf{U}(q_1, q_2, q_3)}{\partial q_l}\mathcal{F}, \tag{17}$$

$$\frac{\partial^2 \mathbf{Q}(z_1, z_2, z_3)}{\partial z_l \partial z_m} = \mathcal{F}^H \frac{\partial^2 \mathbf{U}(q_1, q_2, q_3)}{\partial q_l \partial q_m}\mathcal{F} \tag{18}$$

and, rewriting the rotation terms in (13) as

$$\begin{aligned} \mathbf{R}_l(z_{l+3}) = \mathbf{R}_l(\theta_l) = & \mathcal{F}_{[l+1]_3}^H \mathbf{V}_l^{\tan}(\theta_l)\mathcal{F}_{[l+1]_3} \\ & \mathcal{F}_{[l+2]_3}^H \mathbf{V}_l^{\sin}(\theta_l)\mathcal{F}_{[l+2]_3} \\ & \mathcal{F}_{[l+1]_3}^H \mathbf{V}_l^{\tan}(\theta_l)\mathcal{F}_{[l+1]_3}, \end{aligned} \tag{19}$$

where $[m]_L = (m-1) \bmod L + 1$, by making $l_{+1} = [l+1]_3$ and $l_{+2} = [l+2]_3$,

$$\begin{aligned} & \mathbf{R}_l'(\theta_l) = \\ & \mathcal{F}_{l_{+1}}^H (\mathbf{V}_l'^{\tan}(\theta_l)\mathcal{F}_{l_{+1}}\mathcal{F}_{l_{+2}}^H \mathbf{V}_l^{\sin}(\theta_l)\mathcal{F}_{l_{+2}}\mathcal{F}_{l_{+1}}^H \mathbf{V}_l^{\tan}(\theta_l) + \\ & \quad \mathbf{V}_l^{\tan}(\theta_l)\mathcal{F}_{l_{+1}}\mathcal{F}_{l_{+2}}^H \mathbf{V}_l'^{\sin}(\theta_l)\mathcal{F}_{l_{+2}}\mathcal{F}_{l_{+1}}^H \mathbf{V}_l^{\tan}(\theta_l) + \\ & \quad \mathbf{V}_l^{\tan}(\theta_l)\mathcal{F}_{l_{+1}}\mathcal{F}_{l_{+2}}^H \mathbf{V}_l^{\sin}(\theta_l)\mathcal{F}_{l_{+2}}\mathcal{F}_{l_{+1}}^H \mathbf{V}_l'^{\tan}(\theta_l))\mathcal{F}_{l_{+1}} \end{aligned} \tag{20}$$

and

$$\begin{aligned} & \mathbf{R}_l''(\theta_l) = \\ & \mathcal{F}_{l_{+1}}^H (\mathbf{V}_l''^{\tan}(\theta_l)\mathcal{F}_{l_{+1}}\mathcal{F}_{l_{+2}}^H \mathbf{V}_l^{\sin}(\theta_l)\mathcal{F}_{l_{+2}}\mathcal{F}_{l_{+1}}^H \mathbf{V}_l^{\tan}(\theta_l) + \\ & \quad \mathbf{V}_l^{\tan}(\theta_l)\mathcal{F}_{l_{+1}}\mathcal{F}_{l_{+2}}^H \mathbf{V}_l''^{\sin}(\theta_l)\mathcal{F}_{l_{+2}}\mathcal{F}_{l_{+1}}^H \mathbf{V}_l^{\tan}(\theta_l) + \\ & \quad \mathbf{V}_l^{\tan}(\theta_l)\mathcal{F}_{l_{+1}}\mathcal{F}_{l_{+2}}^H \mathbf{V}_l^{\sin}(\theta_l)\mathcal{F}_{l_{+2}}\mathcal{F}_{l_{+1}}^H \mathbf{V}_l''^{\tan}(\theta_l) + \\ & \quad 2\mathbf{V}_l'^{\tan}(\theta_l)\mathcal{F}_{l_{+1}}\mathcal{F}_{l_{+2}}^H \mathbf{V}_l'^{\sin}(\theta_l)\mathcal{F}_{l_{+2}}\mathcal{F}_{l_{+1}}^H \mathbf{V}_l^{\tan}(\theta_l) + \\ & \quad 2\mathbf{V}_l^{\tan}(\theta_l)\mathcal{F}_{l_{+1}}\mathcal{F}_{l_{+2}}^H \mathbf{V}_l'^{\sin}(\theta_l)\mathcal{F}_{l_{+2}}\mathcal{F}_{l_{+1}}^H \mathbf{V}_l'^{\tan}(\theta_l) + \\ & \quad 2\mathbf{V}_l'^{\tan}(\theta_l)\mathcal{F}_{l_{+1}}\mathcal{F}_{l_{+2}}^H \mathbf{V}_l^{\sin}(\theta_l)\mathcal{F}_{l_{+2}}\mathcal{F}_{l_{+1}}^H \mathbf{V}_l'^{\tan}(\theta_l))\mathcal{F}_{l_{+1}} \end{aligned} \tag{21}$$

Finally, the derivatives of the diagonal elements of $\mathbf{U}$ and $\mathbf{V}_l$ —see (4)— are:

$$\frac{\partial \mathbf{u}(q_1, q_2, q_3)}{\partial q_l} = -j\mathbf{k}_l \circ \mathbf{u}(q_1, q_2, q_3), \tag{22}$$

$$\frac{\partial^2 \mathbf{u}(q_1, q_2, q_3)}{\partial q_l \partial q_m} = -\mathbf{k}_l \circ \mathbf{k}_m \circ \mathbf{u}(q_1, q_2, q_3), \tag{23}$$

$$\begin{aligned} \mathbf{v}_l'^{\tan}(\theta_l) = & j\frac{1 + \tan^2(\theta_l/2)}{2}\mathbf{k}_{l_{+1}} \circ \mathbf{r}_{l_{+2}} \circ \mathbf{v}_l^{\tan}(\theta_l) \\ \mathbf{v}_l'^{\sin}(\theta_l) = & -j\cos(\theta_l)\mathbf{k}_{l_{+2}} \circ \mathbf{r}_{l_{+1}} \circ \mathbf{v}_l^{\sin}(\theta_l) \end{aligned} \tag{24}$$

and

$$\begin{aligned} \mathbf{v}_l''^{\tan}(\theta_l) = & \left(\tan(\theta_l/2) + j\frac{1 + \tan^2(\theta_l/2)}{2}\mathbf{k}_{l_{+1}} \circ \mathbf{r}_{l_{+2}}\right) \circ \\ & \mathbf{v}_l'^{\tan}(\theta_l) \\ \mathbf{v}_l''^{\sin}(\theta_l) = & -(\tan(\theta_l) + j\cos(\theta_l)\mathbf{k}_{l_{+2}} \circ \mathbf{r}_{l_{+1}}) \circ \mathbf{v}_l'^{\sin}(\theta_l) \end{aligned} \tag{25}$$

Then, using the Newton's method, we make:

$$\mathbf{z}^{i+1} = \mathbf{z}^i - \left(w^i \mathbf{Id} + \mathbf{H}^f\right)^{-1} \boldsymbol{\nabla}^f, \tag{26}$$

with i denoting the motion estimation iteration. w^i has been updated according to:

$$w^{i+1} = \begin{cases} 2w^i & \text{if } f(\mathbf{z}^{i+1}) > f(\mathbf{z}^i) \\ w^i/1.2 & \text{otherwise.} \end{cases} \tag{27}$$

This article has been accepted for publication in a future issue of this journal, but has not been fully edited. Content may change prior to final publication. Citation information: DOI 10.1109/TCI.2016.2557069, IEEE Transactions on Computational Imaging

Regarding the stopping criteria, considering that for any transformation $\mathbf{T}_0$, $\mathbf{T}\mathbf{x} = \mathbf{T}\mathbf{T}_0^H\mathbf{T}_0\mathbf{x}$, we introduce a projection step after each motion estimation iteration on which we update $\mathbf{x}^i$ and $\mathbf{T}^i$ according to

$$\begin{aligned} \mathbf{x}^i &\longleftarrow \overline{\mathbf{T}}^i\mathbf{x}^i \\ \mathbf{T}^i &\longleftarrow \mathbf{T}^i\overline{\mathbf{T}}^{iH}, \end{aligned} \tag{28}$$

which does not alter the value of the objective function, and where, following [35],

$$\overline{\mathbf{T}}^i = \mathbf{T}^i\left(\frac{1}{S}\sum_{s=1}^{S}\mathbf{z}_s^i\right), \tag{29}$$

which avoids drifting instabilities in the joint optimization. This way, the stopping condition of the method can be robustly stated using an image-based criterion as

$$\max_n |x_n^{i+1} - x_n^i| < \mu, \tag{30}$$

where n indexes the image voxels and μ is tuned by considering the SNR of the particular application. In our implementation, every joint iteration is in turn comprised of 3 CG iterations and 1 Newton's iteration. However, more sophisticated numerical coupling of motion estimation and reconstruction will likely boost algorithmic performance.

REFERENCES

[1] M. A. Bernstein, K. F. King, and X. J. Zhou, *Handbook of MRI Pulse Sequences*. Elsevier Academic Press, 2004.

[2] J. B. Andre, B. W. Bresnahan, M. Mossa-Basha, M. N. Hoff, C. P. Smith, Y. Anzai, and W. A. Cohen, "Towards quantifying the prevalence, severity, and cost associated with patient motion during clinical MR examinations," *J. Am. Coll. Radiol.*, vol. 12, no. 7, pp. 689–695, Jul. 2015.

[3] J. Budde, G. Shajan, K. Scheffler, and R. Pohmann, "Ultra-high resolution imaging of the human brain using acquisition-weighted imaging at $9.4\,T$," *NeuroImage*, vol. 86, no. 1, pp. 592–598, Feb. 2014.

[4] M. Zaitsev, J. Maclaren, and M. Herbst, "Motion artifacts in MRI: A complex problem with many partial solutions," *J. Magn. Reson. Imaging*, vol. 42, no. 4, pp. 887–901, Oct. 2015.

[5] M. Bydder, D. J. Larkman, and J. V. Hajnal, "Detection and elimination of motion artifacts by regeneration of k-space," *Magn. Reson. Med.*, vol. 47, no. 4, pp. 677–686, Apr. 2002.

[6] A. A. Samsonov, J. Velikina, Y. Jung, E. G. Kholmovski, C. R. Johnson, and W. F. Block, "POCS-enhanced correction of motion artifacts in parallel MRI," *Magn. Reson. Med.*, vol. 63, no. 4, pp. 1104–1110, Apr. 2010.

[7] R. Bammer, M. Aksoy, and C. Liu, "Augmented generalized SENSE reconstruction to correct for rigid body motion," *Magn. Reson. Med.*, vol. 57, no. 1, pp. 90–102, Jan. 2007.

[8] J. G. Pipe, W. N. Gibbs, Z. Li, J. P. Karis, M. Schar, and N. R. Zwart, "Revised motion estimation algorithm for PROPELLER MRI," *Magn. Reson. Med.*, vol. 72, no. 2, pp. 430–437, Aug. 2014.

[9] A. G. Anderson III, J. Velikina, W. Block, O. Wieben, and A. Samsonov, "Adaptive retrospective correction of motion artifacts in cranial MRI with multicoil three-dimensional radial acquisitions," *Magn. Reson. Med.*, vol. 69, no. 4, pp. 1094–1103, Apr. 2013.

[10] A. Loktyushin, H. Nickisch, R. Pohmann, and B. Schölkopf, "Blind retrospective motion correction of MR images," *Magn. Reson. Med.*, vol. 70, no. 6, pp. 1608–1618, Dec. 2013.

[11] ——, "Blind multirigid retrospective motion correction of MR images," *Magn. Reson. Med.*, vol. 73, no. 4, pp. 1457–1468, Apr. 2015.

[12] F. Odille, P.-A. Vuissoz, P.-Y. Marie, and J. Felblinger, "Generalized reconstruction by inversion of coupled systems (GRICS) applied to free-breathing MRI," *Magn. Reson. Med.*, vol. 60, no. 1, pp. 146–157, Jul. 2008.

[13] P. G. Batchelor, D. Atkinson, P. Irarrazaval, D. L. G. Hill, J. Hajnal, and D. Larkman, "Matrix description of general motion correction applied to multishot images," *Magn. Reson. Med.*, vol. 54, no. 5, pp. 1273–1280, Nov. 2005.

[14] M. Unser, P. Thévenaz, and L. Yaroslavsky, "Convolution-based interpolation for fast, high-quality rotation of images," *IEEE Trans. Image Process.*, vol. 4, no. 10, pp. 1375–1381, Oct. 1995.

[15] T. Toffoli and J. Quick, "Three-dimensional rotations by three shears," *Graph. Models. Image Process.*, vol. 59, no. 2, pp. 89–95, Mar. 1997.

[16] M. J. Allison, S. Ramani, and J. A. Fessler, "Accelerated regularized estimation of MR coil sensitivities using augmented Lagrangian methods," *IEEE Trans. Med. Imag.*, vol. 32, no. 3, pp. 556–564, Mar. 2013.

[17] K. P. Pruessmann, M. Weiger, P. Börnert, and P. Boesiger, "Advances in sensitivity encoding with arbitrary k-space trajectories," *Magn. Reson. Med.*, vol. 46, no. 4, pp. 638–651, Oct. 2001.

[18] L.-A. Williams, T. J. DeVito, J. D. Winter, T. N. Orr, R. T. Thompson, and N. Gelman, "Optimization of 3D MP-RAGE for neonatal brain imaging at 3.0 T," *Magn. Reson. Imaging*, vol. 25, no. 8, pp. 1162–1170, Oct. 2007.

[19] E. Hughes, T. Wichmann, L. Mager, F. Padormo, J. Hutter, J. Wurie, M. Fox, M. Sharma, A. D. Edwards, A. Kapetanakis, A. Allievi, and J. Hajnal, "Tackling the challenges of imaging the infant brain in a dedicated neonatal coil," in *Proc. 23rd Ann. Meeting Int. Soc. Magn. Reson. Med.*, Toronto, Canada, May-Jun. 2015, p. 3094.

[20] M. Buehrer, K. P. Pruessmann, P. Boesiger, and S. Kozerke, "Array compression for MRI with large coil arrays," *Magn. Reson. Med.*, vol. 57, no. 6, pp. 1131–1139, Jun. 2007.

[21] Z. Yang, C. Zhang, and L. Xie, "Sparse MRI for motion correction," in *10th IEEE Int. Symp. Biomed. Imaging: From Nano to Macro*, San Francisco, CA, USA, Apr. 2013, pp. 962–965.

[22] K. P. McGee, A. Manduca, J. P. Felmlee, S. J. Riederer, and R. L. Ehman, "Image metric-based correction (autocorrection) of motion effects: Analysis of image metrics," *J. Magn. Reson. Imaging*, vol. 11, no. 2, pp. 174–181, Feb. 2000.

[23] B. Adcock, A. Hansen, B. Roman, and G. Teschke, "Generalized sampling: Stable reconstructions, inverse problems and compressed sensing over the continuum," *Adv. Imag. Electron Phys.*, vol. 182, no. 1, pp. 187–279, 2014.

[24] J. Schulz, T. Siegert, E. Reimer, C. Labadie, J. Maclaren, M. Herbst, M. Zaitsev, and R. Turner, "An embedded optical tracking system for motion-corrected magnetic resonance imaging at $7T$," *Magn. Reson. Mater. Phy.*, vol. 25, no. 6, pp. 443–453, Dec. 2012.

[25] M. Aksoy, C. Forman, M. Straka, T. Çukur, J. Hornegger, and R. Bammer, "Hybrid prospective and retrospective head motion correction to mitigate cross-calibration errors," *Magn. Reson. Med.*, vol. 67, no. 5, pp. 1237–1251, May 2012.

[26] A. Gholipour, J. A. Estroff, and S. K. Warfield, "Robust super-resolution volume reconstruction from slice acquisitions: Application to fetal brain MRI," *IEEE Trans. Med. Imag.*, vol. 29, no. 10, pp. 1739–1758, Oct. 2010.

[27] M. Kuklisova-Murgasova, G. Quaghebeur, M. A. Rutherford, J. V. Hajnal, and J. A. Schnabel, "Reconstruction of fetal brain MRI with intensity matching and complete outlier removal," *Med. Image Anal.*, vol. 16, no. 8, pp. 1550–1564, Dec. 2012.

[28] A. Menini, G. S. Slavin, J. A. Stainsby, P. Ferry, J. Felblinger, and F. Odille, "Motion correction of multi-contrast images applied to T_1 and T_2 quantification in cardiac MRI," *Magn. Reson. Mater. Phy.*, vol. 28, no. 1, pp. 1–12, Feb. 2015.

[29] L. Cordero-Grande, S. Merino-Caviedes, S. Aja-Fernández, and C. Alberola-López, "Groupwise elastic registration by a new sparsity-promoting metric: Application to the alignment of cardiac magnetic resonance perfusion images," *IEEE Trans. Pattern Anal. Mach. Intell.*, vol. 35, no. 11, pp. 2638–2650, Nov. 2013.

[30] S. G. Lingala, E. DiBella, and M. Jacob, "Deformation corrected compressed sensing (DC-CS): A novel framework for accelerated dynamic MRI," *IEEE Trans. Med. Imag.*, vol. 34, no. 1, pp. 72–85, Jan. 2015.

[31] J. Royuela-del-Val, L. Cordero-Grande, F. Simmross-Wattenberg, M. Martín-Fernández, and C. Alberola-López, "Non-rigid groupwise registration for motion estimation and compensation in compressed sensing reconstruction of breath-hold cardiac cine MRI," *Magn. Reson. Med.*, vol. 75, no. 4, pp. 1525–1536, Apr. 2016.

[32] R. Winkelmann, P. Börnert, and O. Dössel, "Ghost artifact removal using a parallel imaging approach," *Magn. Reson. Med.*, vol. 54, no. 4, pp. 1002–1009, Oct. 2005.

[33] L. Ying and J. Sheng, "Joint image reconstruction and sensitivity estimation in SENSE (JSENSE)," *Magn. Reson. Med.*, vol. 57, no. 6, pp. 1196–1202, Jun. 2007.

This article has been accepted for publication in a future issue of this journal, but has not been fully edited. Content may change prior to final publication. Citation information: DOI 10.1109/TCI.2016.2557069, IEEE Transactions on Computational Imaging

[34] J. M. Peeters and M. Fuderer, "SENSE with improved tolerance to inaccuracies in coil sensitivity maps," *Magn. Reson. Med.*, vol. 69, no. 6, pp. 1665–1669, Jun. 2013.

[35] K. K. Bhatia, J. V. Hajnal, B. K. Puri, A. D. Edwards, and D. Rueckert, "Consistent groupwise non-rigid registration for atlas construction," in *IEEE International Symposium on Biomedical Imaging: Nano to Macro*, Arlington, USA, Apr. 2004, pp. 908–911.

Lucilio Cordero-Grande received the Ingeniero de Telecomunicación, Postgraduate Certificate in Education, and Ph.D. degrees from the University of Valladolid, Valladolid, Spain, in 2005, 2009, and 2012, respectively. He was a Research Associate at the Laboratory of Image Processing (LPI) of the Universidad de Valladolid from 2005 to 2013. Since then, he is a Research Associate at the Centre for the Developing Brain and Department of Biomedical Engineering, King's College London. His research interests include applied functional analysis, statistical and variational methods for biomedical image processing and reconstruction.

Rui Pedro A. G. Teixeira received his BSc in Engineering Sciences and MSc in Biomedical Engineering and Biophysics degrees from the University of Lisbon, Lisbon, Portugal, in 2011 and 2013, respectively. Since 2013 he has undertaken a PhD studentship at the Department of Imaging Sciences and Biomedical Engineering of King's College London. His research interests include design and optimization of quantitative and qualitative MRI techniques.

Emer J. Hughes attained a BSc in mathematics, physics and biology and a Higher Diploma in Education (St Patrick's College, Maynooth, Republic of Ireland). She was a teacher of science for 8 years completing her MSc in Educational management (Queens College , Belfast) in 2000. She then went on to attain a BSc in Diagnostic Medical Imaging (Christ Church University College, Canterbury) and received her PhD from Imperial College London in 2013. Since 2012 she has worked at the Centre for the Developing Brain at Kings College London as the lead radiographer for the developing Human Connectome Project.

Jana Hutter did her undergraduate degrees in applied mathematics and received a Ph.D. from the University of Erlangen-Nuremberg in 2014. Since 2014 she is an associate researcher at the Centre for the Developing Brain at King's College London. Her interest include MRI physics, sequence development, diffusion MRI as well as fetal and neonatal imaging.

Anthony N. Price received his BSc in medical physics and PhD in MRI physics degrees from the University of Nottingham in 2002 and 2006, respectively. Subsequently he been a research fellow at Imperial College, University College London, and since 2012, the Division of Imaging Sciences and Biomedical Engineering at King's College London. His research interests include developing MRI techniques for neuro and cardiovascular applications in fetal and neonatal subjects.

Joseph V. Hajnal obtained a BSc and PhD in Physics from the University of Bristol, UK. Since 1990 his research has focused on medical image acquisition, reconstruction and analysis, mostly related to MRI. He was head of the Imaging Sciences Department at Imperial College and a group leader and head of section at the MRC Clinical Research Centre. He is a fellow of the ISMRM and is currently Professor of Imaging Science at King's College London.